# Numerical Investigation of Slag Entrainment in Continuous Casting Molds

Kenneth E. Swartz,[1] Lance C. Hibbeler,[1] Brendan P. Joyce,[2] and Brian G. Thomas [1]

1 - The University of Illinois at Urbana–Champaign
Department of Mechanical Science and Engineering
1206 West Green Street (MC 244), Urbana, Illinois, USA, 61801-2906

2 - The University of Illinois at Urbana–Champaign
Department of Nuclear, Plasma, and Radiological Engineering
104 South Wright Street (MC 234), Urbana, Illinois, USA, 61801-2983

Phone: +1-217-333-6919 (B. G. Thomas)
Email: swartz6@illinois.edu, lhibbel2@illinois.edu, BrendanJoyce6@gmail.com, bgthomas@illinois.edu

Keywords: Slag entrainment, continuous casting, computational model, model verification and validation

## ABSTRACT

This article presents a three-dimensional, transient, multiphase, turbulent numerical model of slag entrainment in continuous casting molds. The model uses explicit time marching, the volume-of-fluid method with the geometric-reconstruction scheme for multiphase phenomenona, and the $k$-$\omega$ turbulence model. The numerical model is verified with analytical solutions, and then is validated with experiments of a rotating cylinder submerged in a tank of oil and water. These experiments report the critical angular velocity of the cylinder at which oil entrainment starts to occur, and the model reasonably agrees.

## 1. INTRODUCTION

Mold slag entrainment, *i.e.*, liquid mold powder being drawn into the melt, is a challenge to the production of clean steel. The literature identifies nine mechanisms [1,2] of mold slag entrainment, shown in Figure 1:

1. top surface fluctuations,
2. meniscus freezing/hook formation,
3. vortex formation in the wake of the submerged entry nozzle,
4. shear-layer instability,
5. **upward flow impinging upon the top surface**,
6. argon bubble interactions/slag foaming,
7. slag crawling down the submerged entry nozzle,
8. top surface stationary wave instability, and
9. top surface "balding."

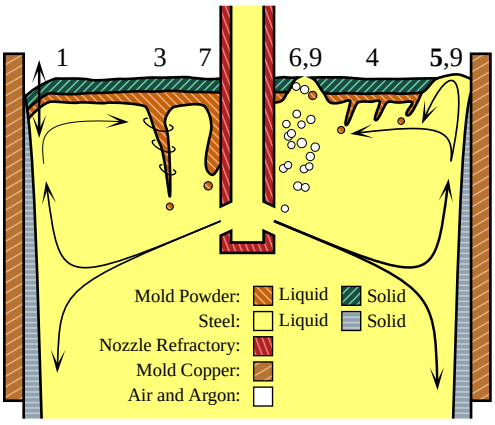


Figure 1. Slag entrainment mechanisms [1,2]

Entrainment depends upon the mass density, dynamic shear viscosity, and interfacial tension of the involved fluids. The orientation of the slag-steel interface relative to the direction of gravity also affects entrainment.

This work explores the "upward flow impinging upon the top surface" entrainment mechanism. Section 2 critically reviews the relevant previous studies. Section 3 describes the numerical model used in this work to investigate slag entrainment, which is verified and validated in Sections 4 and 5. Future work will use this validated model to explore entrainment in slag-steel systems and metallurgical processes. The ultimate goal of this work is to relate the tendency for entrainment with casting conditions such as casting speed, argon gas flow rate, submerged entry nozzle design and operation, and mold dimensions.

## 2. PREVIOUS STUDIES OF SLAG ENTRAINMENT

The previous studies of slag entrainment have used theoretical models, oil-water physical models, and numerical models. These studies explored the critical speed $V_{\text{crit}}$ at or near the liquid interface at which entrainment occurs; speeds in excess of this critical value result in slag entrainment. In this article, $\rho$ is mass density, $\mu$ is dynamic shear viscosity, $\nu = \mu/\rho$ is kinematic shear viscosity, $\Gamma$ is interfacial tension, $h$ is a layer thickness, and $g$ is the acceleration due to gravity. Subscripts u refer to the upper fluid, *i.e.*, oil or slag, and subscripts $\ell$ refer to the lower fluid, *i.e.*, water or steel. The numerical constants in the equations presented in this section expect that all quantities are given in m-kg-s units, *i.e.*, mass density in kg/m$^3$, dynamic shear viscosity in Pa s, interfacial tension in N/m, and layer thickness in m, to give speed in m/s.

### 2.1. Theoretical Models

An analysis of the stability of the interface between two parallel-flowing, stratified fluids,[3,4] shown in Figure 2, gives the critical entrainment speed as

$$\frac{V_{\text{crit}}}{\sqrt[4]{g\Gamma_{u\ell}/\rho_u}} = \sqrt[4]{4}\sqrt{1+\frac{\rho_u}{\rho_\ell}}\sqrt[4]{\frac{1}{\rho_u/\rho_\ell}-1}, \tag{1}$$

assuming that the upper fluid is at rest. The speed necessary for instability depends on the size of the perturbation to the interface, and Equation (1) occurs at the capillary wavelength,

$$\lambda_c = 2\pi\sqrt{\frac{\Gamma_{u\ell}}{g\left(\rho_\ell-\rho_u\right)}}, \tag{2}$$

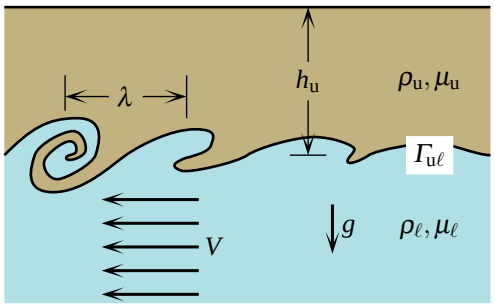


Figure 2. Shear instability model[3,4,5]

where the effects of interfacial tension and gravity are balanced. The analysis underlying Equation (1) assumed irrotational and inviscid fluids in an infinite domain; the latter two assumptions were relaxed[5] to give

$$V_{\text{instability}}(\lambda) = \sqrt{\left(g\left(\rho_\ell-\rho_u\right)\frac{\lambda}{2\pi}+\Gamma_{u\ell}\frac{2\pi}{\lambda}\right)\frac{\left(\mu_\ell+\mu_u\coth\left(\frac{2\pi}{\lambda}h_u\right)\right)^2}{\left(\rho_u\coth\left(\frac{2\pi}{\lambda}h_u\right)\right)\mu_\ell^2+\rho_\ell\left(\mu_u\coth\left(\frac{2\pi}{\lambda}h_u\right)\right)^2}}, \tag{3}$$

assuming that the lower fluid is infinite. The critical speed predicted by Equation (3) is found by minimizing the equation with respect to the perturbation wavelength $\lambda$, which occurs at a wavelength of about $(1\pm0.005)\,\lambda_c$. The viscous model predicts a lower critical speed than the inviscid model because of the momentum transport by shear stresses. The upper fluid effectively is infinite in this model when $h_u \gtrsim 3\lambda_c/2\pi$, or about 27 mm for oil-water systems and 15 mm for slag-steel systems. The phenomenon illustrated in Figure 2 has long been under investigation; many other theoretical and experimental treatments[6,7,8] are found in the literature.

One model proposed that entrainment occurs when the kinetic energy of a spherical droplet, $E_K$, exceeds the sum of the energy cost of forming the surface area, $E_S$, and the work done by the buoyancy force through a distance of one-half of the droplet diameter, $W_B$, *i.e.*, the work done to pull a droplet out of the slag layer.[9] The critical entrainment speed predicted by this model is

$$\frac{V_{\text{crit}}}{\sqrt[4]{g\Gamma_{u\ell}/\rho_u}} = \sqrt[4]{48}\sqrt[4]{\frac{1}{\rho_u/\rho_\ell}-1}. \tag{4}$$

A similar analysis based on forces[10,11] instead of energies predicts that the critical entrainment speed is

$$\frac{V_{\text{crit}}}{\sqrt[4]{g\Gamma_{u\ell}/\rho_u}} = \sqrt[4]{\frac{128}{3}\cos(\phi)}\sqrt[4]{\frac{1}{\rho_u/\rho_\ell}-1}, \tag{5}$$

where $\phi$ is the angle of the liquid interface relative to the direction of gravity, as shown in Figure 3. The critical speed from Equation (5) always is less than that from Equation (4). For a horizontal interface, *i.e.*, $\phi = 90°$, the critical speed from Equation (5) is zero, which indicates some error in the model.

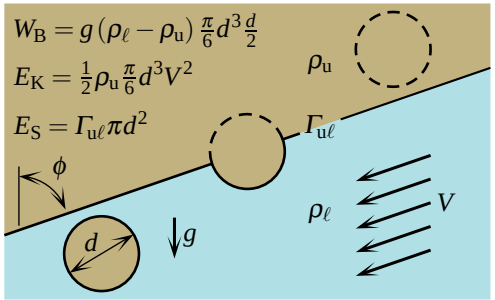


Figure 3. Droplet entrainment model[9,10,11]

### 2.2. Oil-Water Physical Models

One experimental apparatus used a submerged hose that was aimed at a vertical wall in a rectangular tank,[12,13] shown in Figure 4. Measurements were made using laser-image velocimetry (LIV). The original results[12] from the hose apparatus were reduced to the expression

$$V_{\text{crit}} = c\frac{\Gamma_{\text{u}\ell}^{1.037}}{g^{0.012}}\frac{(\rho_\ell-\rho_{\text{u}})^{0.239}}{\rho_{\text{u}}^{0.227}}\frac{\mu_{\text{u}}^{0.321}}{\mu_\ell^{1.370}}, \tag{6}$$

where $c = 1.2\times10^{-3}$ is a dimensionless constant. An extended study[13] with the hose apparatus produced the expression

$$V_{\text{crit}} = c\frac{\Gamma_{\text{u}\ell}^{0.292}g^{0.115}}{h_{\text{u}}^{0.365}}\frac{(\rho_\ell-\rho_{\text{u}})^{0.215}}{\rho_{\text{u}}^{0.694}}\frac{\mu_{\text{u}}^{0.231}}{\mu_\ell^{0.043}} \tag{7}$$

where $c = 3.065$ is a dimensionless constant.

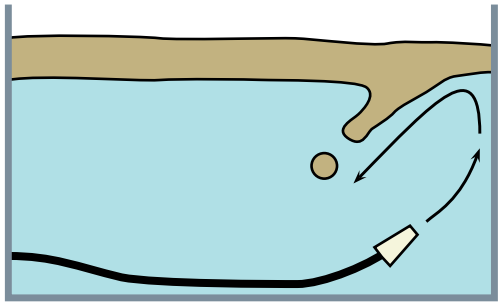

Figure 4. Hose apparatus[12,13]

Another experimental apparatus used a submerged rotating cylinder in a rectangular tank,[14,15] shown in Figure 5. The measured critical speeds were reduced to a critical capillary number $\text{Ca} = \mu V/\Gamma$ as a function of the ratio of kinematic shear viscosities $\nu_{\text{u}}/\nu_\ell$. An early study[14] measured the tangential velocity of the surface of the cylinder and proposed the model

$$V_{\text{crit}} = c_1\frac{\Gamma_{\text{u}\ell}}{\mu_\ell}\exp\left(c_2\frac{\nu_{\text{u}}}{\nu_\ell}\right), \tag{8}$$

where $c_1 = 0.0233$ and $c_2 = 0.001$ are dimensionless constants. Because Equation (8) gives very large speeds, a later study[15] used particle-image velocimetry (PIV) to measure the water speed 2 mm away from the surface of the cylinder and proposed the model

$$V_{\text{crit}} = \frac{\Gamma_{\text{u}\ell}}{\mu_\ell}\left(c_1 + c_2\frac{\nu_{\text{u}}}{\nu_\ell}\right) \tag{9}$$

where $c_1 = 2.8\times10^{-3}$ and $c_2 = 3\times10^{-6}$ are dimensionless constants.

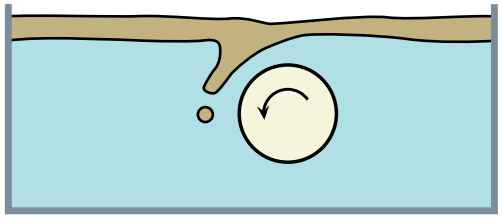

Figure 5. Cylinder apparatus[14,15]

Another study used a ramp/weir submerged in a rectangular tank,[16] shown in Figure 6. Measurements were made with PIV. These researchers did not propose a model, but did explore a wide range of properties.

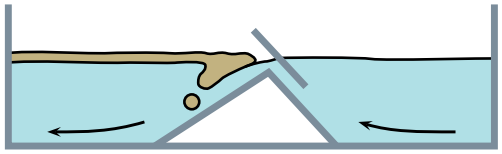

Figure 6. Ramp apparatus[16]

Gas-stirred ladles have flow phenomena similar to molds that cause entrainment. In ladles, entrainment often is desirable because of the increase in slag-steel interfacial area and corresponding increase in mass transfer during stirring. The main difference between entrainment in a ladle and in a mold, from a fluid-mechanic perspective, is that ladle slag layers are about 10 times thicker than mold slag layers. Many studies of ladles have explored a critical gas flow rate.[10,11,17] Because of various difficulties with measurements in round vessels, other studies used a rectangular ladle-like apparatus,[11,18,19,20,21] shown in Figure 7, to explore the critical interface speed. One study[21] with laser-Doppler velocimetry (LDV) measured a critical entrainment speed of 0.233 m/s, and the researchers proposed, based on this single data point, that entrainment occurs at a Weber number $\text{We} = \rho V^2 L/\Gamma$ of 12.3, using the lower-fluid density and characteristic length of $L = \lambda_{\text{c}}/2\pi$, which gives the critical entrainment speed as

$$V_{\text{crit}} = \sqrt[4]{151.3\Gamma_{\text{u}\ell}\frac{g\,(\rho_\ell-\rho_{\text{u}})}{\rho_\ell^2}}. \tag{10}$$

Another study with a similar ladle-like apparatus[18,19,20] measured with PIV a critical entrainment speed of 0.264 m/s. The oil speeds near the interface were observed[18,19,20] to be about 1/10 as much as the speeds in the water. Another study[11] supported the predictions of Equation (5) and its accompanying droplet size model at speeds greater than the critical.

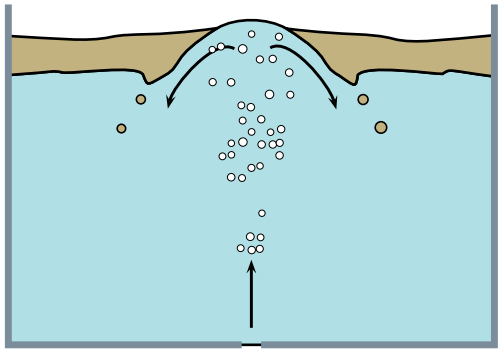

Figure 7. Ladle-like apparatus[11,18,19,20,21]

The shear instability phenomenon shown in Figure 2 has been explored experimentally by using a rotating trough,[6,7,8,22] as shown in Figure 8. These experiments offer controllable conditions to investigate the behavior of the fluid interface, but the finite-ness of the domain limits the applicability of the measurements in metallurgical processes.

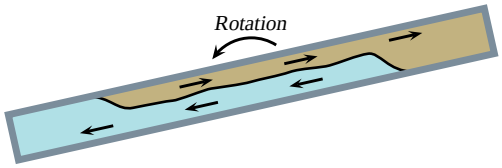


Figure 8. Rotating trough apparatus[6,7,8,22]

### 2.3. Numerical Models

The shear-layer instability shown in Figure 2 was investigated for a slag-steel system with a temperature gradient through the slag layer and temperature dependent properties.[1] This investigation observed degrees of instability of the interface, *i.e.*, that the interface can be considered unstable without entraining droplets, and found that slag entrainment occurred at about 1.1 m/s.

Three-dimensional (3D) large-eddy simulations[23,24] of the flow in the ramp apparatus shown in Figure 6 explored the entrained droplet creation rate[24] and size distribution.[23,24] The two-phase model[24] used both oil-water and slag-steel systems, and the three-phase model[23] used air, oil, and water. These models underpredict the experimentally-observed[16] droplet diameters by a factor of 2 or more, but indicate that the droplet size distribution is insensitive to the fluid-system material properties.

An axisymmetric, argon-slag-steel multiphase numerical model of heat transfer and turbulent fluid flow in a ladle[25] supports Equation (10). A two-dimensional (2D), oil-water multiphase numerical model of turbulent fluid flow in the ladle-like apparatus[18,26] shown in Figure 7 predicts[18] a critical entrainment speed of $(0.24 \pm 0.02)$ m/s, which agrees with the $(0.26 \pm 0.04)$ m/s that was measured[18,19,20] in the apparatus. However, this simulation used an eddy viscosity model specialized for jets, and not a general-purpose turbulence model.

### 2.4. Comparison and Evaluation of Previous Work

The quantitative agreement of the models in the literature is poor. Using the material properties listed in Table I, the critical entrainment speeds predicted by the models discussed in this section are presented in Table II. If needed, the upper-layer thickness is $h_u = 10$ mm, and the angle of the interface from gravity is $\phi = 60°$. The predicted entrainment speeds vary widely, particularly in the slag-steel system, though the property values are reasonable; these models should be applied carefully outside of the conditions for which they were developed. The disagreement among models can be explained by: differences in interface geometry, the sensitivity of the phenomenon to interfacial tension, and measurement technique. Additionally, the observation that the fluid in the upper layer is not at rest[18,19,20] affects the reliability of the theoretical model predictions.

Figure 9 evaluates eight of the models presented in this section with the available measurements. The measurements from the ramp apparatus[16] perhaps are subject to some systematic error. The theoretical models are about as accurate as could be expected, and the empirical models work well only for the measurements to which they were fit. Fitting measurements against a single dimensionless number, *e.g.*, Equations (8), (9), and (10), or a product of several dimensionless numbers, *e.g.*, Equations (6) and (7), oversimplifies the problem and sheds little light on the underlying physics of entrainment. Dimensionless quantities like the Weber number are intended to be used as order-of-magnitude quantifications of flow regimes. Empirical models may be used for plant practice, but the scatter presented in Figure 9 casts reasonable doubt on all of the models reviewed in this section. Across all the data, Equation (7) seems to be the best fit with an error of about $\pm 25\%$.

Table I. Typical values of fluid-system properties used in literature model comparisons

| System | Mass Density | | | Dynamic Shear Viscosity | | | Kinematic Shear Viscosity | | | Interfacial Tension | Characteristic Velocity | Capillary Wavelength |
|---|---|---|---|---|---|---|---|---|---|---|---|---|
| | $\rho_u$ | $\rho_\ell$ | $\rho_u/\rho_\ell$ | $\mu_u$ | $\mu_\ell$ | $\mu_u/\mu_\ell$ | $\nu_u$ | $\nu_\ell$ | $\nu_u/\nu_\ell$ | $\Gamma_{u\ell}$ | $\sqrt[4]{g\Gamma_{u\ell}/\rho_u}$ | $\lambda_c$ |
| | kg/m$^3$ | | – | mPa s | | – | mm$^2$/s | | – | mN/m | m/s | mm |
| Oil–Water | 960 | 997 | 0.963 | 50 | 0.9 | 50 | 52.1 | 1.00 | 52.0 | 30 | 0.132 | 56.4 |
| Slag–Steel | 2500 | 7200 | 0.347 | 300 | 5 | 60 | 120 | 0.694 | 173 | 1100 | 0.256 | 30.7 |

Table II. Literature model predictions of critical entrainment speed in m/s

| System | *Theoretical Models* | | | | *Experimental Models* | | | | |
|---|---|---|---|---|---|---|---|---|---|
| | Eq. (1)[3,4] | Eq. (3)[5] | Eq. (4)[9] | Eq. (5)[11] | Eq. (6)[12] | Eq. (7)[13] | Eq. (8)[14] | Eq. (9)[15] | Eq. (10)[21] |
| Oil–Water | 0.116 | 0.0825 | 0.154 | 0.126 | 0.0873 | 0.0963 | 0.823 | 0.0991 | 0.202 |
| Slag–Steel | 0.493 | 0.254 | 0.790 | 0.645 | 1.59 | 0.565 | 6.09 | 0.730 | 0.620 |

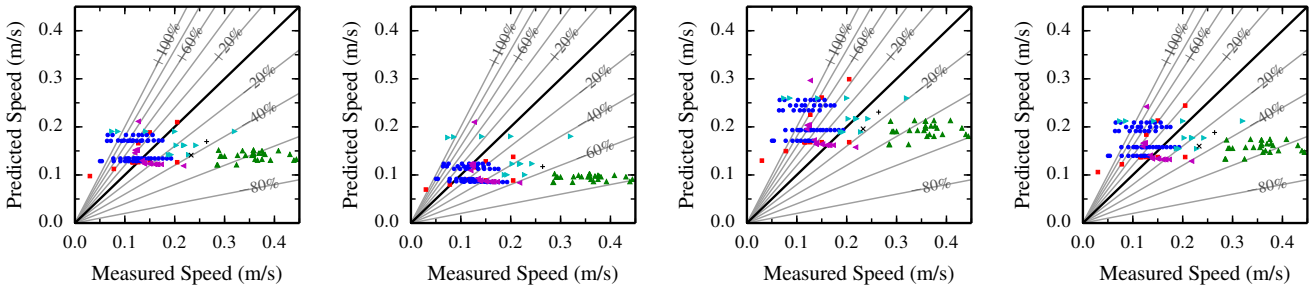


(a) Equation (1)[3,4] (b) Equation (3)[5] (c) Equation (4)[9] (d) Equation (5)[11]

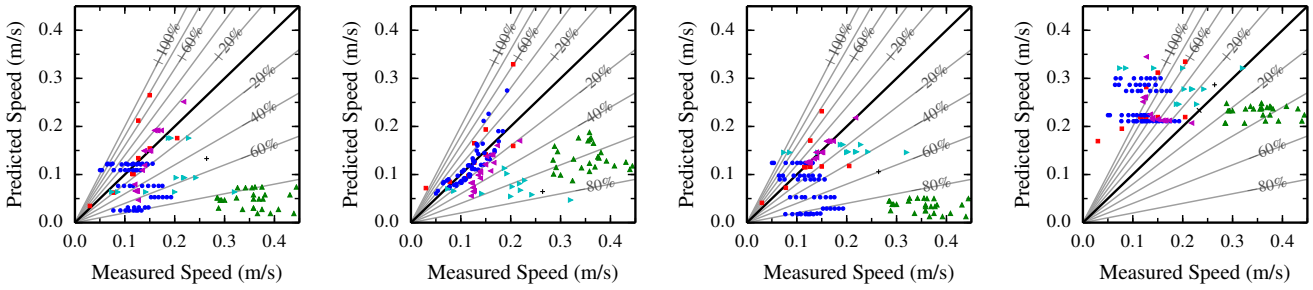


(e) Equation (6)[12] (f) Equation (7)[13] (g) Equation (9)[15] (h) Equation (10)[21]

Figure 9. Evaluation of literature models for available data. Measurements are from the hose apparatus: ■[12] and ●,[13] the cylinder apparatus: ◀,[15] the ramp apparatus: ▲,[16] ladle apparatuses: +[18,19,20] and ×,[21] and the rotating trough apparatus: ▶.[22]

Qualitatively, the previous experimental studies are in good agreement. The critical entrainment speed has been observed:

- to increase with increasing interfacial tension,[12,13,16]
- to increase with increasing difference in density between the upper and lower fluids,[12,13,16]
- to increase with increasing ratio of kinematic shear viscosities,[14,15,17]
- to increase with increasing upper-layer dynamic shear viscosity,[12,13,15,16]
- to increase with,[16] to decrease with,[13,17] and to be independent of,[15] the upper layer thickness.

However, in experiments it is difficult to change independently each material property. The diameter of the entrained droplets has been observed:

- to increase with increasing interfacial tension,[12,15,16]
- to increase with decreasing difference in density between the upper and lower fluids,[12,16]
- to increase with increasing ratio of kinematic shear viscosities,[14,15]
- to increase with increasing upper-layer dynamic shear viscosity,[12,16] and
- to increase with[16] and to be independent of[13] the upper-layer thickness.

Most researchers[11,12,13,16,17] measure the diameter of the entrained oil droplets in the range 5 mm to 10 mm, but others[15] have reported diameters as large as 30 mm. Quantitative knowledge of droplet size is useful for calculating post-entrainment droplet behavior in molds and ladles, and for predicting the enhancement to mass transfer during stirring in ladles.

The inviscid energetic model, Equation (4), intuitively is an upper bound for entrainment, which is of little practical use. The theoretical models suggest that $\lambda_c$ and $\sqrt[4]{g\Gamma_{u\ell}/\rho_u}$ are the characteristic length and speed for interfacial phenomena; the characteristic time then is $\lambda_c/\sqrt[4]{g\Gamma_{u\ell}/\rho_u}$. Analysis of experimental data demonstrated that measurements scale well with this speed.[17] Though the functional relationship remains to be determined, the best course of action seems to be a fit of the form

$$\frac{V_{crit}}{\sqrt[4]{g\Gamma_{u\ell}/\rho_u}} = f\left(\frac{\rho_u}{\rho_\ell}, \frac{h_u}{\lambda_c}, \mu_u, \mu_\ell, \phi\right), \tag{11}$$

where $f = 0$ at $\rho_u/\rho_\ell = 1$, and the dependence of $f$ on $h_u/\lambda_c$ should monotonically and asymptotically tend toward "no effect" as $h_u/\lambda_c$ increases. In any case, future work on this subject should report the complete data set $\{V_{crit}, \rho_u, \rho_\ell, \mu_u, \mu_\ell, \Gamma_{u\ell}, h_u, \phi\}$ for each measurement. Given the stochastic nature of the phenomenon, any future effort also must include enough repeated measurements so that sound statistical conclusions may be drawn.

## 3. DESCRIPTION OF NUMERICAL MODEL OF SLAG ENTRAINMENT

The slag entrainment phenomenon is explored in this work with a numerical model because *in situ* investigations are prohibitively difficult and the previous work is lacking. The theoretical treatments simplify the physics for the sake of achieving a closed-form solution, and oil-water physical models do not satisfy all of the necessary similarity criteria and are subject to experimental variability. Numerical modeling offers precise control over the physics and boundary conditions, and omniscient knowledge of the state of the system, though the technique is not without its shortcomings, such as turbulence modeling and mesh resolution.

This section presents the transient, multiphase, turbulent numerical model used in this work to explore the slag entrainment phenomenon. This model is verified in Section 4, and is validated in Section 5 with data from the cylinder apparatus shown in Figure 5. The model is implemented with the commercial software FLUENT.[27]

### 3.1. Governing Equations and Boundary Conditions

The equations that govern the motion of fluids,[28] written for a spatial description of motion at an arbitrary point $\boldsymbol{x}$ and instant of time $t$, are the conservation of mass,

$$\frac{\partial \rho}{\partial t} + \nabla \cdot (\rho \boldsymbol{v}) = 0, \tag{12}$$

and the conservation of momentum,

$$\frac{\partial (\rho \boldsymbol{v})}{\partial t} + \nabla \cdot (\rho \boldsymbol{v} \otimes \boldsymbol{v}) = -\nabla p + \nabla \cdot \boldsymbol{\tau} + \boldsymbol{b}, \tag{13}$$

where $\rho(\boldsymbol{x},t)$ is the mass density, $\boldsymbol{v}(\boldsymbol{x},t)$ is the velocity vector, $p(\boldsymbol{x},t)$ is the pressure, $\boldsymbol{\tau}(\boldsymbol{x},t)$ is the deviatoric part of the Cauchy stress tensor, and $\boldsymbol{b}(\boldsymbol{x},t)$ is the body force density vector.

The boundary conditions on the mass and momentum equations either are a specified velocity, or "no-slip" condition,

$$\boldsymbol{v} = \boldsymbol{v}^{\text{sp}}, \tag{14}$$

where the specified velocity $\boldsymbol{v}^{\text{sp}}$ is zero on stationary walls and is an appropriate non-zero value on moving walls, or a specified traction,

$$-p\boldsymbol{n} + \boldsymbol{n} \cdot \boldsymbol{\tau} = \boldsymbol{t}^{\text{sp}}, \tag{15}$$

where $\boldsymbol{n}$ is the outward-pointing unit normal vector of a surface, and $\boldsymbol{t}^{\text{sp}}$ is the specified traction. On no-shear walls, the shear part of the the traction, $\boldsymbol{n} \cdot \boldsymbol{\tau}$, is zero.

The body force density vector caused by gravity is $\boldsymbol{b}^{\text{g}} = g(\rho - \rho_{\text{ref}})\boldsymbol{e}^{\text{g}}$, where $\rho_{\text{ref}}$ is the reference density and $\boldsymbol{e}^{\text{g}}$ is the unit vector pointing in the direction of gravity. The reference density is taken as $\rho_{\text{ref}} = 0$ in this work.

### 3.2. Constitutive Relationship (Turbulence Model)

The deviatoric part of the Cauchy stress tensor $\boldsymbol{\tau}$ is assumed to follow the incompressible Newtonian constitutive relationship,

$$\boldsymbol{\tau} = 2\mu \boldsymbol{D}, \tag{16}$$

where $\mu(\boldsymbol{x},t)$ is the dynamic shear viscosity of the fluid and $\boldsymbol{D}(\boldsymbol{x},t)$ is the rate-of-deformation tensor, defined as

$$\boldsymbol{D} = \frac{1}{2}\left(\nabla \boldsymbol{v} + (\nabla \boldsymbol{v})^T\right). \tag{17}$$

For turbulent flows, use of Equation (16) is impractical, and so the continuity and momentum equations are ensemble-averaged to give the Reynolds-averaged Navier–Stokes (RANS) equations. The RANS form of the continuity and momentum equations are identical to Equations (12) and (13) with the velocity vector $\boldsymbol{v}$ interpreted as a time-averaged velocity, using an averaging window larger than the time scale of the turbulent eddies but smaller than the time scale of the bulk flow features. The Reynolds-averaging process creates additional terms in the stress tensor, which must be "closed" with a turbulence model. The turbulence closure model adopted in this work is the two-equation shear-stress transport (SST) $k$-$\omega$ model,[29] including the default model constants. The constitutive relationship for this model is

$$\boldsymbol{\tau} = 2(\mu + \mu_{\text{t}})\boldsymbol{D} - \frac{2}{3}\rho k \boldsymbol{I}, \tag{18}$$

where $\mu_t$ is the eddy viscosity, $k$ is the specific turbulent kinetic energy (TKE), and $\boldsymbol{I}$ is the second-order identity tensor. The eddy viscosity is computed with

$$\mu_t = \rho k \Big/ \max\left(\frac{\omega}{q}, \frac{\dot{\gamma} F}{0.31}\right), \tag{19}$$

where $\omega$ is the specific turbulent dissipation rate (TDR), $\dot{\gamma} = \sqrt{2\boldsymbol{D}:\boldsymbol{D}}$ is the magnitude of the averaged rate-of-deformation tensor, $F(k,\omega)$ is a blending function, and

$$q = (0.144 + \mathrm{Re}_t)\,/\,(6 + \mathrm{Re}_t), \tag{20}$$

with $\mathrm{Re}_t = \rho k/\mu\omega$ as the turbulent Reynolds number, is a "transitional," *i.e.*, low-Reynolds-number, damping factor.

The specific turbulent kinetic energy $k(\boldsymbol{x},t)$ is governed by

$$\frac{\partial(\rho k)}{\partial t} + \nabla\cdot(\rho k\boldsymbol{v}) = \nabla\cdot\left(\left(\mu + \frac{\mu_t}{\mathrm{Pr}_{tk}}\right)\nabla k\right) + S_k, \tag{21}$$

and the specific turbulent dissipation rate $\omega(\boldsymbol{x},t)$ is governed by

$$\frac{\partial(\rho\omega)}{\partial t} + \nabla\cdot(\rho\omega\boldsymbol{v}) = \nabla\cdot\left(\left(\mu + \frac{\mu_t}{\mathrm{Pr}_{t\omega}}\right)\nabla\omega\right) + S_\omega, \tag{22}$$

where $\mathrm{Pr}_{tk}(k,\omega)$ and $\mathrm{Pr}_{t\omega}(k,\omega)$ are the turbulent Prandtl numbers for the $k$ and $\omega$ fields. The details of $F$, $\mathrm{Pr}_{tk}$, $\mathrm{Pr}_{t\omega}$, the model production/dissipation source terms $S_k(k,\omega)$ and $S_\omega(k,\omega)$, and the boundary conditions on the $k$ and $\omega$ fields are left to the references.[27,29] The turbulence model is implemented with curvature corrections[27] because of the geometry considered in this work. The specific TKE is initialized to

$$k(\boldsymbol{x}, t=0) = \tfrac{3}{2}(IV)^2, \tag{23}$$

where $I = 0.05$ is the assumed turbulent intensity and $V$ is the characteristic speed of the problem. The specific turbulent dissipation rate is initialized such that $\mu_t = m_t\mu$, where $m_t = 10$ is the initial turbulent-to-laminar dynamic shear viscosity ratio. Manipulating Equations (19) and (20), the initial specific TDR is calculated as

$$\omega(\boldsymbol{x}, t=0) = \frac{\rho k}{\mu}\frac{1}{2}\left(\frac{0.144 - m_t}{6m_t} + \sqrt{\left(\frac{0.144 - m_t}{6m_t}\right)^2 + \frac{4}{6m_t}}\right). \tag{24}$$

### 3.3. Multiphase Model

At the interface between fluids A and B, the boundary conditions[28] consist of local kinematic continuity,

$$\boldsymbol{v}^A = \boldsymbol{v}^B, \tag{25}$$

and a local momentum balance,

$$-\left(p^A - p^B\right)\boldsymbol{n}^{AB} + \left(\boldsymbol{\tau}^A - \boldsymbol{\tau}^B\right)\cdot\boldsymbol{n}^{AB} = 2\kappa_m\Gamma_{AB}\boldsymbol{n}^{AB} + \left(\boldsymbol{I} - \boldsymbol{n}^{AB}\otimes\boldsymbol{n}^{AB}\right)\cdot\nabla\Gamma_{AB}, \tag{26}$$

where $\boldsymbol{n}^{AB}(\boldsymbol{x},t)$ is the unit normal vector at the interface that points from fluid A to fluid B, and $\Gamma_{AB}(\boldsymbol{x},t)$ is the interfacial tension between the fluids. The mean curvature $\kappa_m(\boldsymbol{x},t)$ of the interface is defined as

$$2\kappa_m = (1/R_1) + (1/R_2), \tag{27}$$

where $R_1(\boldsymbol{x},t)$ and $R_2(\boldsymbol{x},t)$ are the principal radii of curvature of the fluid interface. The last term in Equation (26) is the interfacial force generated by gradients of surface tension. This force is neglected in this work, though it is relevant to slag entrainment in metallurgical processes because interfacial tension strongly depends on temperature and chemical composition.

Multiphase phenomena are modeled with the volume-of-fluid (VOF) method.[30] For the two distinct fluids water and oil, the VOF method introduces two scalar fields, $f_{oil}(\boldsymbol{x},t)$ and $f_{water}(\boldsymbol{x},t)$, that represent the volume of each fluid within an averaging region. All fluids share one velocity field, which satisfies the kinematic continuity condition, Equation (25). Water is taken as the primary phase because it is the more-dense fluid, so the oil volume-fraction field is subject to a mass balance,

$$\frac{\partial(f_{oil}\rho_{oil})}{\partial t} + \nabla\cdot(f_{oil}\rho_{oil}\boldsymbol{v}) = 0. \tag{28}$$

The two volume fraction fields must partition unity, so the volume fraction of water is calculated with

$$f_{\text{water}} = 1 - f_{\text{oil}}, \tag{29}$$

for all positions $\boldsymbol{x}$ and times $t$, rather than solving another differential equation like Equation (28).

The material properties are taken as volume-weighted averages of the individual fluid properties: the average mass density $\bar{\rho}$ is

$$\bar{\rho} = f_{\text{water}}\rho_{\text{water}} + f_{\text{oil}}\rho_{\text{oil}}, \tag{30}$$

and the average dynamic shear viscosity $\bar{\mu}$ is

$$\bar{\mu} = f_{\text{water}}\mu_{\text{water}} + f_{\text{oil}}\mu_{\text{oil}}. \tag{31}$$

The mass and momentum equations, Equations (12) and (13), and the turbulence field equations, Equations (21) and (22), use $\bar{\rho}$ for the mass density and $\bar{\mu}$ for the dynamic shear viscosity. The fluids in this work are considered as incompressible, but the full continuity equation is used because the density at a point in space can change as the flow evolves.

Interfacial tension effects are modeled with the continuum surface force (CSF) method.[31] The CSF method creates a new body force $\boldsymbol{b}^{\Gamma}$ in the momentum balance that is a diffuse-interface approximation of the effects of interfacial tension, calculated as

$$\boldsymbol{b}^{\Gamma} = 2\kappa_{\text{m}}\Gamma_{\text{oil-water}}\left(\nabla f_{\text{oil}}\frac{\bar{\rho}}{\frac{1}{2}\left(\rho_{\text{oil}}+\rho_{\text{water}}\right)}\right). \tag{32}$$

The mean curvature of the interface between the fluids $\kappa_{\text{m}}$ is calculated with

$$2\kappa_{\text{m}} = \nabla\cdot\boldsymbol{n}^{\text{oil-water}}, \tag{33}$$

rather than trying to compute the principal curvatures of the interface and then using Equation (27) for the mean curvature. The unit normal vector of the interface is computed from the volume-fraction field as

$$\boldsymbol{n}^{\text{oil-water}} = \nabla f_{\text{oil}}/\left\|\nabla f_{\text{oil}}\right\|. \tag{34}$$

At solid walls, the fluid interface normal is calculated as $\boldsymbol{n}^{\text{oil-water}} = \boldsymbol{n}^{\text{w}}\cos(\theta_{\text{w}}) + \boldsymbol{t}^{\text{w}}\sin(\theta_{\text{w}})$, where $\boldsymbol{n}^{\text{w}}$ and $\boldsymbol{t}^{\text{w}}$ are the unit vectors normal to and tangent with the wall, and $\theta_{\text{w}}$ is the wetting angle. The wetting angle is taken as $\theta_{\text{w}} = 90^{\circ}$ because of the lack of wetting angle measurements for the fluids used in this work.

An additional source term in the $\omega$ turbulence equation damps out the turbulence generated at the interface of two fluids[27] because of the large velocity gradient across the interface:

$$S^{\Gamma} = 480B^2\frac{\mu_{\text{oil}}^2}{\rho_{\text{oil}}}\frac{A_{\text{oil}}}{\Delta n^3}, \tag{35}$$

where $B = 10$ is a damping factor, $\Delta n$ is the cell height normal to the interface, and $A_{\text{oil}} = 2f_{\text{oil}}\left\|\nabla f_{\text{oil}}\right\|$ is the interfacial area density of the oil phase.

### 3.4. Discretization and Solution Methods

The governing equations are discretized with the finite volume method (FVM) and then are solved on a fixed, unstructured grid. In the momentum, turbulent kinetic energy, and turbulent dissipation rate equations, the advective terms are discretized with the second-order upwind scheme and the diffusive terms are discretized with the second-order central scheme. Velocities and turbulence quantities are modeled at cell centers, and pressure is modeled at cell-face centers; this staggering* of the pressure computes pressure gradients more accurately than co-locating the pressure and velocity, particularly at boundaries. Cell-face quantities, namely the flux quantities, are computed as the face-average value of the quantity at the nodes, which are computed from weighted averages of the values in the surrounding cells.†

The volume fraction equations are discretized with the explicit geometric-reconstruction scheme,[32] generalized for unstructured meshes.[27] This method is more accurate and less diffuse than other methods, which is explored in Section 4.2. The averaging region mentioned in Section 3.3 is taken as the volume of a cell, so the volume of oil in a cell is calculated as $V_{\text{oil}} = f_{\text{oil}}V_{\text{cell}}$.

*In FLUENT, this method is referred to as the pressure staggering option, or the PRESTO method. This method is a generalization to unstructured meshes of the staggered pressure technique found in textbooks on computational fluid dynamics.

†In FLUENT, this method is referred to as the Green–Gauss node-based method for gradient quantities. This approach has been demonstrated to be more accurate for unstructured meshes than the usual approach of taking the arithmetic mean of adjacent cell-center values.[27]

Pressure-velocity coupling is treated with the pressure-implicit splitting of operators (PISO) method,[33] using a single neighbor-correction iteration. Using the PISO method allows the under-relaxation factors for the pressure, momentum, and turbulence equations to be taken as unity. The reference pressure in the pressure-correction equation is taken as 101 325 Pa and is located at $\boldsymbol{x}^{\text{ref}}$. Transient simulations are solved using first-order non-iterative time advancement. The time step is determined during the simulation by keeping the largest Courant number $C = \|\boldsymbol{v}\| / (\Delta x/\Delta t)$ less than some maximum value $C_{\max}$.

## 4. MODEL VERIFICATION

Model verification evaluates programming/implementation fidelity by comparing the solution computed by the numerical model with an analytical solution of a simple test problem. Verification also allows easy exploration of appropriate time steps, mesh sizes, and other model parameters. Two test problems are employed in this work to verify the numerical model: tangential annular drag flow and a two-fluid axially-rotating cylinder.

### 4.1. Tangential Annular Drag Flow

The single-phase verification problem considers long, concentric rotating cylinders at steady state, or "tangential annular drag flow," shown in Figure 10. The problem conditions are listed in Table III. For this problem, the Reynolds number, $\text{Re} = \rho V L/\mu$, is calculated with the characteristic speed as the tangential velocity of the inner cylinder, $V = R_{\text{i}}\Omega_{\text{i}}$, and the characteristic length as the distance between cylinders, $L = R_{\text{o}} - R_{\text{i}}$. The entire annulus was discretized with 10 329 quadrilateral cells, using 33 cells in the radial direction and 313 cells around the circumference.

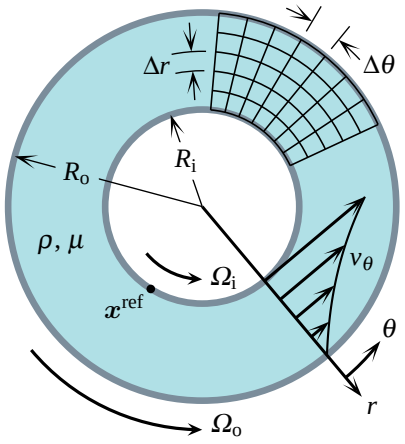


Figure 10. Domain, boundary conditions, and part of mesh for the tangential annular drag flow test problem

Table III. Conditions for tangential annular drag flow test problem

| Quantity | Symbol | Value | Unit |
|---|---|---|---|
| Outer cylinder radius | $R_{\text{o}}$ | 40 | mm |
| Inner cylinder radius | $R_{\text{i}}$ | 20 | mm |
| Outer cylinder angular velocity | $\Omega_{\text{o}}$ | 0 | rad/s |
| Inner cylinder angular velocity | $\Omega_{\text{i}}$ | 0.1 | rad/s |
| Acceleration due to gravity | $g$ | 0 | m/s$^2$ |
| Mass density | $\rho$ | 997 | kg/m$^3$ |
| Dynamic shear viscosity | $\mu$ | 0.9 | mPa s |
| Reynolds number | Re | 44 | – |
| Analytical solution constant 1 | $c_1$ | −0.0333 | 1/s |
| Analytical solution constant 2 | $c_2$ | 53.3 | mm$^2$/s |
| Radial mesh size | $\Delta r$ | 0.606 | mm |
| Circumferential mesh size | $\Delta\theta$ | 0.0201 | rad |
| Reference pressure location | $\boldsymbol{x}^{\text{ref}}$ | (20,0) | mm |

The numerical solution and analytical solution[28] for laminar flow with water are compared in Figure 11. All residual norms in the numerical solution were reduced to machine precision in about 17 000 iterations. The analytical solution, given in Figure 11, has $v_r = 0$, $v_\theta = v_\theta(r)$, $v_z = 0$, and $p = p(r)$. The numerical model matches the analytical solution for the tangential velocity to $7.2 \times 10^{-4}$ mm/s (0.2%) or less and the tangential-radial shear stress to $3.4 \times 10^{-3}$ mPa ($2.7 \times 10^{-4}$%) or less at every node. The radial pressure gradient matches the analytical solution to 0.55 mPa/m (1.0%) or less at every node more than 2 mm from the inner wall. A larger error is seen near the inner wall because of the calculation of the discrete derivative during post-processing.

The behavior of this problem in turbulent flow is explored by increasing the angular velocity of the inner cylinder to 1, 5, and 10 rad/s, with other conditions kept the same as in Table III. As shown in Figure 12 for five turbulence models, boundary layers develop near the walls, and are about 5 mm thick for fully-developed turbulence. For this problem, these five RANS models are in good agreement: the $k$-$\omega$ models predict larger boundary layers and about 5% smaller wall stresses than the $k$-$\varepsilon$ models.

### 4.2. Two-Fluid Rotating Cylinder

The two-phase, transient verification problem considers air and water in an axially-rotating cylinder, shown in Figure 13. The problem conditions are listed in Table IV. For this problem, the Reynolds numbers are calculated with the characteristic speed as the tangential velocity of the cylinder, $V = R\Omega$, and the characteristic length as the radius of the cylinder, $L = R$. An axisymmetric plane of the cylinder was discretized with 31 250 quadrilateral cells, using 125 cells in the radial direction and 250 cells in the axial direction.

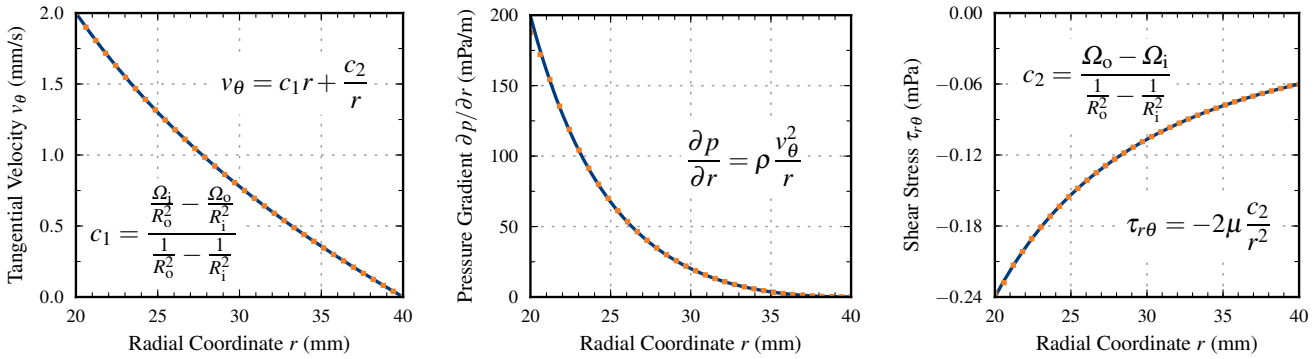


Figure 11. Verification of numerical model (▪) with analytical solution (—) for laminar tangential annular drag flow

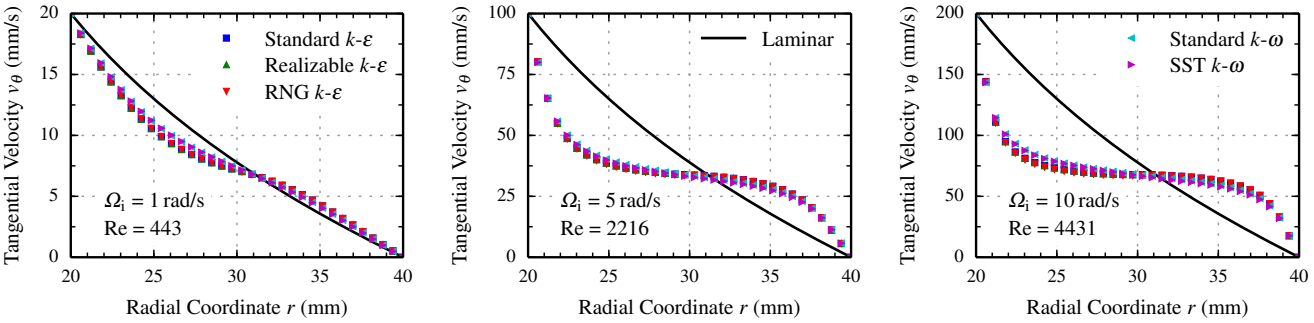


Figure 12. Tangential annular drag flow problem at higher speeds with different turbulence models

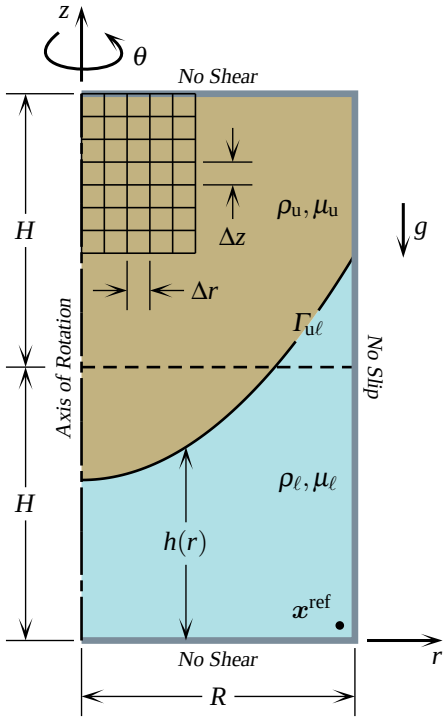


Figure 13. Domain, boundary conditions, and part of mesh for the two-fluid test problem

Table IV. Rotating cylinder test problem conditions

| Quantity | Symbol | Value | Unit |
|---|---|---|---|
| Cylinder half-height | $H$ | 50 | mm |
| Cylinder radius | $R$ | 50 | mm |
| Cylinder angular velocity | $\Omega$ | 18 | rad/s |
| Outer surface tangential velocity | $R\Omega$ | 0.9 | m/s |
| Acceleration due to gravity | $g$ | 9.807 | m/s$^2$ |
| Upper fluid mass density | $\rho_u$ | 1.225 | kg/m$^3$ |
| Lower fluid mass density | $\rho_\ell$ | 997 | kg/m$^3$ |
| Upper fluid dynamic shear viscosity | $\mu_u$ | 17.9 | μPa s |
| Lower fluid dynamic shear viscosity | $\mu_\ell$ | 0.9 | mPa s |
| Interfacial tension | $\Gamma_{u\ell}$ | 0 | N/m |
| Upper fluid Reynolds number | $\mathrm{Re}_u$ | 3080 | – |
| Lower fluid Reynolds number | $\mathrm{Re}_\ell$ | 49 850 | – |
| Initial specific TKE | $k_0$ | 3.04 | mJ/kg |
| Upper fluid initial specific TDR | $\omega_{u0}$ | 14.7 | 1/s |
| Lower fluid initial specific TDR | $\omega_{\ell 0}$ | 238 | 1/s |
| Radial mesh size | $\Delta r$ | 0.400 | mm |
| Axial mesh size | $\Delta z$ | 0.400 | mm |
| Maximum Courant number | $C_{max}$ | 0.4 | – |
| Reference pressure location | $\boldsymbol{x}^{ref}$ | (49,1) | mm |

The numerical solution and analytical solution are compared in Figure 14, which shows the calculated volume-fraction field at 100 s. Steady-state calculations did not converge, regardless of the VOF discretization method and mesh size, so the simulation was integrated through time until steady-state conditions were achieved. The numerical and analytical interface shapes are in good agreement, and the model conserves mass very well: the volume of the water increased by $1.53 \times 10^{-4}\%$ over the course of the time marching.

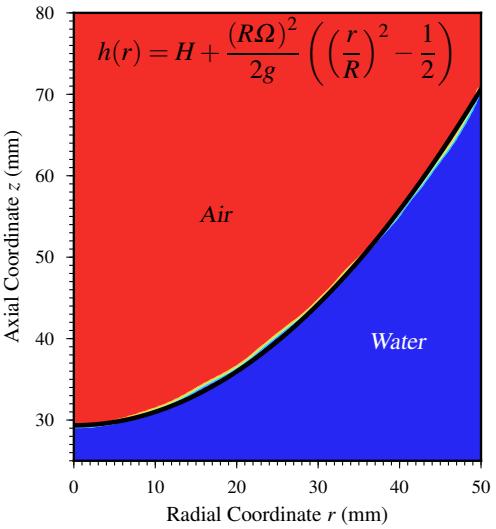


Figure 14. Verification of numerical model (contours) with analytical solution (black line) for interface shape

The geometric-reconstruction scheme used for the volume-fraction field in this model does not suffer from excessive numerical diffusion like other methods. The spread of the calculated interface, defined as $0.01 \leq f_{\text{water}} \leq 0.99$, is shown in Figure 15 for four different mesh resolutions at 2 s, with all other simulation conditions kept the same as in Table IV. Regardless of the mesh size, the interface is spread across three cells. The results of this mesh study are crucial for interpreting the model results: to resolve fully the dynamics of a droplet of diameter $d$ requires cell sizes of about $d/10$. For larger cells, the model is computing the average behavior of a fluid mixture, and nothing can be claimed about surface interactions with the droplet. However, the diameter of the oil droplet within a cell of volume $V_{\text{cell}}$ can be estimated as

$$d = \sqrt[3]{(6/\pi)\, f_{\text{oil}} V_{\text{cell}}}. \tag{36}$$

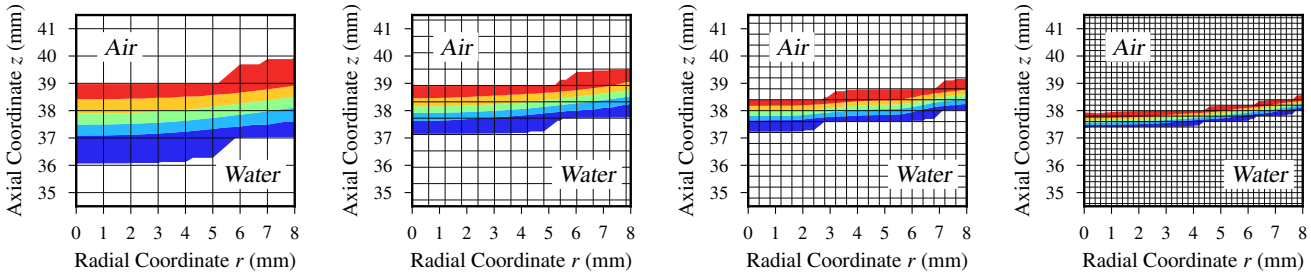


(a) $50 \times 100 = 5000$ cells, $\Delta r = \Delta z = 1$ mm

(b) $83 \times 167 = 13861$ cells, $\Delta r = \Delta z = 0.6$ mm

(c) $125 \times 250 = 31250$ cells, $\Delta r = \Delta z = 0.4$ mm

(d) $250 \times 500 = 125000$ cells, $\Delta r = \Delta z = 0.2$ mm

Figure 15. Mesh study for multiphase model (VOF with explicit geometric-reconstruction scheme)

## 5. MODEL VALIDATION

Model validation evaluates the ability of the model to duplicate experimental measurements. Validation ensures that the numerical model contains appropriate physics and boundary conditions. The numerical model presented in Section 3 is validated in this section with data from the cylinder apparatus [15] shown in Figure 5. The most reliable data from that experimental study are the angular velocities of the cylinder at the onset of entrainment, hereafter called the "critical angular velocities," which are used in this work as the validation targets.

### 5.1. Oil-Water Model Description

The domain and boundary conditions in the numerical model, shown in Figure 16, mirror the experiments. The domain is a 3D rectangular tank with an axially-rotating cylinder inside of it. A layer of oil rests on top of a bath of water and the cylinder rotates with increasing angular velocity to induce entrainment. The domain is discretized with 102 360 hexahedral cells, with an edge length of about 2 mm and cell volume of $V_{\text{cell}} = 8.7\,\text{mm}^3$. The problem conditions are summarized in Table V, and the properties for the four oils used in this work are given in Table VI. The 3D simulations in this work were computed on a 6-core, 2.67 GHz workstation and required about a week per simulation.

The top wall boundary condition is either a no-slip wall, *i.e.*, a closed tank, to simulate a solid powder layer, or a no-shear wall, *i.e.*, an open tank, to simulate a free surface. The experimentalists reported insignificant differences in entrainment behavior between the two top wall conditions. [15]

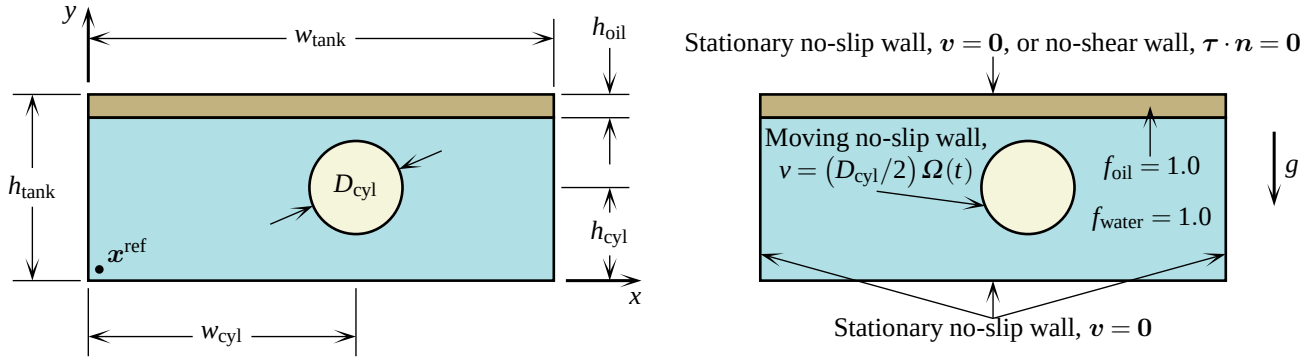


Figure 16. Domain, boundary, and initial conditions for model validation simulations

The angular velocity of the cylinder is prescribed as

$$\Omega(t) = \begin{cases} \Omega_0 & \text{if } 0 \le t \le t_0 \\ \Omega_0 + \alpha\,(t - t_0) & \text{if } t_0 \le t \end{cases}, \tag{37}$$

where $\Omega_0$ = 18 rad/s is the angular velocity applied for $t_0$ = 200 s to establish an initial steady state. From this steady state, the cylinder is accelerated with angular acceleration $\alpha$ = 0.05 rad/s$^2$ until entrainment occurs. The angular velocity evolution is plotted in Figure 17. The experimentalists found[15] that entrainment behavior is independent of angular acceleration for $\alpha = 0.05\,\text{rad/s}^2$. In the numerical model, the time-dependent velocity of the cylinder surface is applied with a FLUENT user-defined function as

$$v_x = -\left(D_{cyl}/2\right)\Omega \sin(\theta) \tag{38}$$

$$v_y = \left(D_{cyl}/2\right)\Omega \cos(\theta) \tag{39}$$

$$v_z = 0, \tag{40}$$

with $\Omega$ calculated from Equation (37) and the angle $\theta$ calculated from the coordinates of a point on the surface of the cylinder as

$$\theta = \text{atan2}\left(y - h_{cyl}, x - w_{cyl}\right). \tag{41}$$

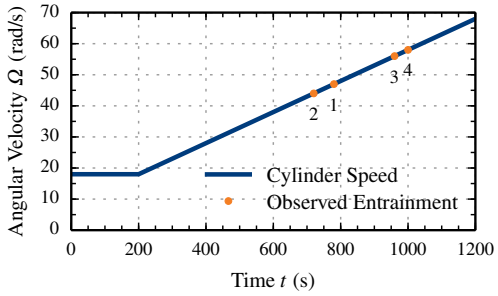


Figure 17. Angular velocity of cylinder

Table V. Conditions for model validation simulations

| Quantity | Symbol | Value | Unit |
|---|---|---|---|
| Tank width | $w_{tank}$ | 200 | mm |
| Tank height | $h_{tank}$ | 80 | mm |
| Tank thickness | $t_{tank}$ | 60 | mm |
| Cylinder horizontal position | $w_{cyl}$ | 115 | mm |
| Cylinder vertical position | $h_{cyl}$ | 40 | mm |
| Cylinder diameter | $D_{cyl}$ | 40 | mm |
| Oil layer thickness | $h_{oil}$ | 10 | mm |
| Acceleration due to gravity | $g$ | 9.807 | m/s$^2$ |
| Maximum Courant number | $C_{max}$ | 0.4 | – |
| Reference pressure location | $\boldsymbol{x}^{ref}$ | (1,1,1) | mm |

Table VI. Fluid properties from cylinder apparatus experiments[15]

| Fluid | Mass Density | | Dynamic Shear Viscosity | | Kinematic Shear Viscosity | | Interfacial Tension |
|---|---|---|---|---|---|---|---|
| | $\rho$ | $\rho_u/\rho_\ell$ | $\mu$ | $\mu_u/\mu_\ell$ | $\nu$ | $\nu_u/\nu_\ell$ | $\Gamma_{u\ell}$ |
| | kg/m$^3$ | – | mPa s | – | mm$^2$/s | – | mN/m |
| Water | 997 | | 0.9 | | 0.903 | | |
| Oil 1 | 920 | 0.923 | 4.6 | 5.1 | 5.0 | 5.5 | 40 |
| Oil 2 | 930 | 0.933 | 9.3 | 10 | 10 | 11 | 40 |
| Oil 3 | 963 | 0.966 | 96.0 | 107 | 99.7 | 110 | 42 |
| Oil 4 | 966 | 0.969 | 193 | 214 | 200 | 221 | 44 |

### 5.2. Oil-Water Model Results

The initial validation efforts simulated a 2D slice through the center of the tank. An entrained "droplet" in two dimensions is a cylinder, so the interfacial tension was taken as zero to cancel this error. Entraining a cylinder is more difficult than entraining a sphere because of the larger surface area, and the previous work discussed in Section 2 showed that entrainment is easier with lower interfacial tension. Under these conditions, for Oil 2, the simulated critical angular velocity overpredicts the measurement

by 6.5% for a no-slip top wall. If interfacial tension is included in the 2D simulation, entrainment does not occur for a no-slip top wall boundary condition, and for a no-shear top wall the simulated critical angular velocity overpredicts the measurement by 0.15%. With interfacial tension and a no-slip top wall boundary condition, the simulated oil layer broke into two distinct sections, which was not observed in the experiments.[15]

The 3D simulations are in good agreement with the experimental measurements for the lower-viscosity oils, as shown in Table VII. The oil layer in the simulations broke apart at about $x = 160$ mm; although the layer did not break in the experiments,[15] the simulation results still are valid near the cylinder. The volume of water increased by $6.59 \times 10^{-5}$% over the simulation.

Table VII. Measured and calculated critical cylinder angular velocities in rad/s

| Fluid | Closed Tank (No-Slip Top Wall) | | Open Tank (No-Shear Top Wall) | |
|---|---|---|---|---|
| | *Measured* | *Calculated* | *Measured* | *Calculated* |
| Oil 1 | $46 \pm 2$ | 48 | $47 \pm 2$ | 43 |
| Oil 2 | $46 \pm 2$ | 44 | $44 \pm 2$ | 40 |
| Oil 3 | $53 \pm 2$ | $*$ | $56 \pm 3$ | $*$ |
| Oil 4 | $59 \pm 1$ | $*$ | $58 \pm 1$ | |

$*$ – Oil layer broke into two distinct sections

The critical angular velocities reported in Table VII were determined by examining the behavior of the $f_{\text{oil}} = 0.05$ iso-surface. Using Equation (36), this value of oil volume-fraction with cells 2 mm on a side corresponds to an oil droplet diameter of about 1 mm. According to the mesh study in Section 4.2, this mesh can resolve droplets of about 20 mm diameter.

For Oil 2, using a no-slip top wall and the described entrainment criterion, the model underpredicts the measured critical angular velocity by about 4%. The critical entrainment speed, measured 3.5 mm from the $f_{\text{oil}} = 0.5$ iso-surface, is 0.2 m/s, which is comparable to values reported in Section 2. Figure 18 shows a 2D slice of the $f_{\text{oil}}$ contours from 0.01 to 1.00 at $z = 36.5$ mm relative to the back face of the tank. This figure looks similar to the photographs of the experiments[15] shown in Figure 19. These photographs are for an oil with $\nu_u/\nu_\ell = 50$, while the simulated oil in Figure 18 has $\nu_u/\nu_\ell = 10$. The simulations calculate that the droplet formation occurs over 0.1 s, while the experimentalists[15] report about 4 s; other experimental work[18,19,20,26] reports about 0.3 s for the droplet formation time. Figure 20 shows an end-view with the same conditions as Figure 18 with the $f_{\text{oil}} = 0.03$ iso-surface shown for clarity. Both of these figures show a finger-like protrusion from the oil layer immediately

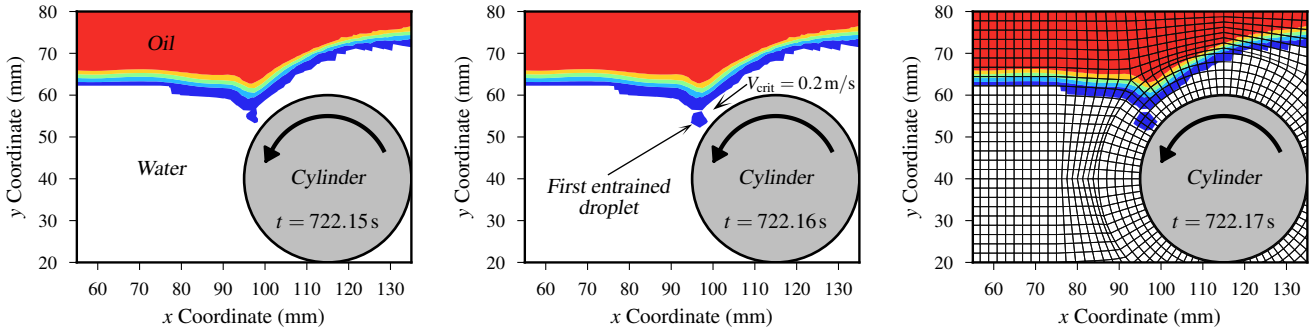


Figure 18. Section view of validation domain at $z = 35.5$ mm, showing Oil 2 entrainment at $\Omega = 44.1$ rad/s

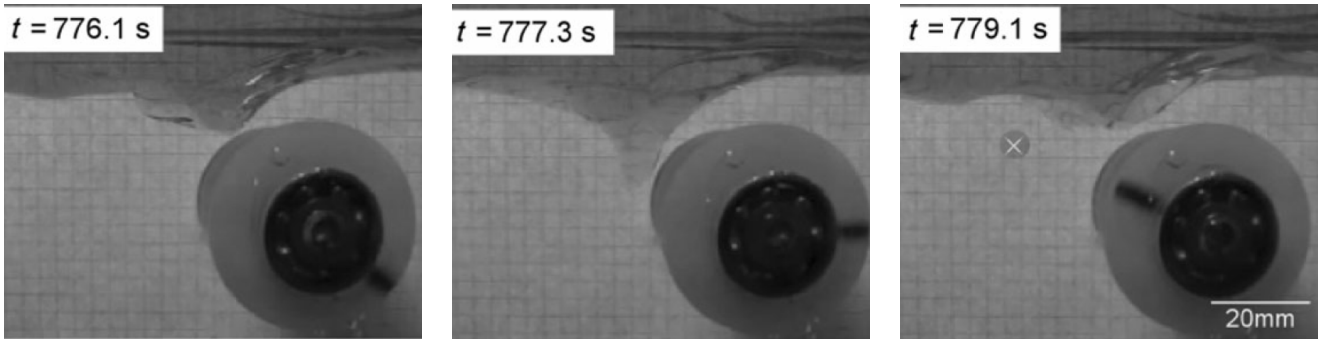


Figure 19. Photographs of entrainment experiments (From Figure 5 of Reference 15)

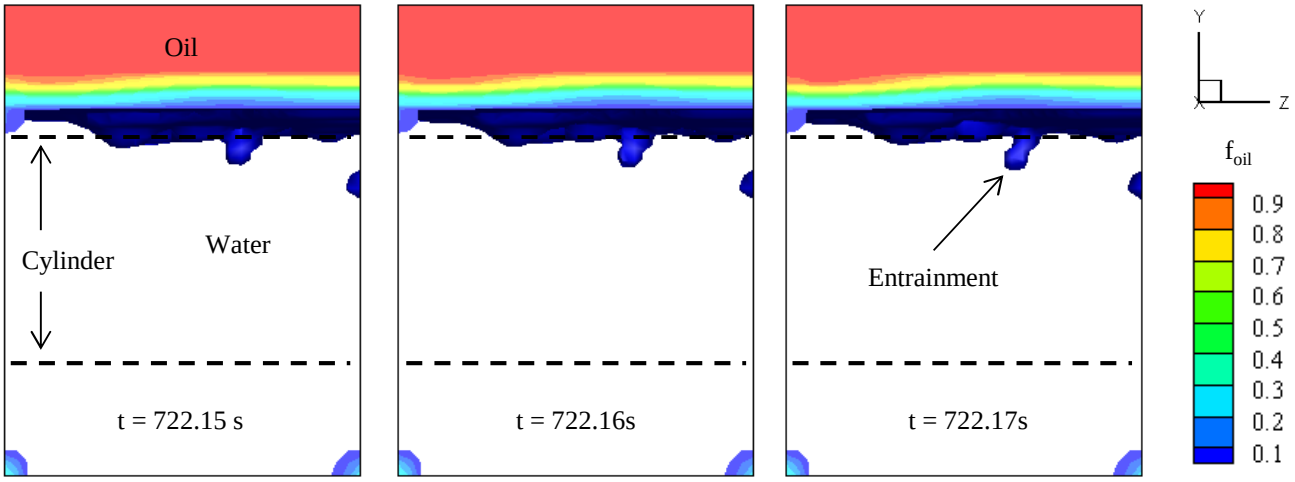


Droplets accumulating unrealistically in bottom corners

Figure 20. End view of validation domain from $x = 0$ mm, showing Oil 2 entrainment at $\Omega = 44.1$ rad/s

prior to droplet formation; this behavior was observed in almost all of the cited previous experimental studies. In Figure 20, the brightly-colored region is the oil touching the wall and the shaded region is the perspective view of the deformed oil-water interface. Repeating the simulation with a no-shear top wall underpredicts the measured critical angular velocity by about 9%.

The critical angular velocities reported in Table VII correspond to the first entrained droplet that is not in contact with the cylinder or the walls. Droplets were entrained at and moved along the walls at lower angular velocities than the reported values, but these droplets are considered as numerical artifacts because of the assumption of a wetting angle of 90° and the coarse mesh. These erroneous droplets accumulate in the lower corners of the tank, as shown in Figure 20. Future modeling work should resolve these issues by including a realistic wetting angle and a more refined mesh near the walls.

The simulations of Oils 3 and 4, as well as an oil with $\nu_u/\nu_\ell = 50$, do not match the experiments. The oil layer breaks into two sections, leaving no oil within about one $D_{cyl}$ of the center of the cylinder, which is denoted with an $*$ in Table VII. The no-shear top wall boundary condition has not been simulated for Oil 4 because the same result is expected. When the oil-water interface comes too close to the top wall, the 90° wetting angle causes the oil to spread even farther apart. This error could be corrected by refining the mesh or using a three-phase model with a layer of air on top of the oil to remove this boundary effect. Future modeling work should explore why the model, as it stands, cannot correctly simulate the behavior of the most viscous oil.

## 6. CONCLUSIONS

A three-dimensional, transient, two-phase numerical model of turbulent fluid flow has been developed for oil-water or slag-steel systems to predict entrainment. The model uses the geometric-reconstruction volume-of-fluid (VOF) scheme with the shear-stress transport (SST) k-$\omega$ turbulence model in FLUENT. The VOF results with a coarse mesh should be interpreted appropriately by looking at low volume-fraction iso-surfaces. The model has been verified with the analytical solutions of laminar tangential annular drag flow and the shape of the air-water interface in an axially-rotating cylinder. The model has been validated with experiments of oil entrainment into water caused by a rotating cylinder: the 3D model matches the measured values to within 4% or 9%, depending on the boundary condition on the top of the oil layer. However, more work is recommended to improve the model-predicted behavior regarding breakup of the interface, especially for more viscous oils. This model is ready to apply in the investigation of slag entrainment in metallurgical systems, with appropriate properties for the slag and steel.

## ACKNOWLEDGMENTS

The financial support of the members of the Continuous Casting Consortium at the University of Illinois at Urbana–Champaign is acknowledged gratefully. At the time of writing, the members are: ABB, ArcelorMittal, Baosteel, Magnesita Refractories, Nippon Steel and Sumitomo Metal Corporation, Nucor Steel Decatur, POSTECH/POSCO, Severstal, SSAB, Tata Steel, and ANSYS-FLUENT. The authors also thank Professor S. P. Vanka and Mr. Rui Liu, both at UIUC, for helpful discussions about the numerical simulations in this work.

## REFERENCES


1. L. C. Hibbeler, R. Liu, and B. G. Thomas, "Review of mold flux entrainment mechanisms and model investigation of entrainment by shear-layer instability," in *Proceedings of the 7th European Continuous Casting Conference*, Steel Institute VDEh, 2011.
2. L. C. Hibbeler and B. G. Thomas, "Mold slag entrainment mechanisms in continuous casting molds," *Iron and Steel Technology*, vol. 8, no. 10, pp. 121–136, 2013.
3. H. L. F. von Helmholtz, "Über discontinuierliche Fluеßigkeits-Bewegungen," *Monatsberichte der Königlichen Preußische Akademie der Wissenschaften zu Berlin*, vol. 23, pp. 215–228, 1868.
4. W. Thomson, "Hydrokinetic solutions and observations," *Philosophical Magazine*, vol. 42, no. 281, pp. 362–377, 1871.
5. T. Funada and D. D. Joseph, "Viscous potential flow analysis of Kelvin–Helmholtz instability in a channel," *Journal of Fluid Mechanics*, vol. 445, pp. 263–283, 2001.
6. S. A. Thorpe, "On standing internal gravity waves of finite amplitude," *Journal of Fluid Mechanics*, vol. 32, no. 3, pp. 489–528, 1968.
7. S. A. Thorpe, "Experiments on the instability of stratified shear flows: Immiscible fluids," *Journal of Fluid Mechanics*, vol. 39, no. 1, pp. 25–48, 1969.
8. S. A. Thorpe, "Experiments on the instability of stratified shear flows: Miscible fluids," *Journal of Fluid Mechanics*, vol. 46, no. 2, pp. 299–319, 1971.
9. S. Asai, "Fluid flow and mass transfer in metallurgical processes where stirring is utilized," in *Proceedings of the 100th and 101st Nishiyama Memorial Lecture*, pp. 65–100, The Iron and Steel Institute of Japan, 1984.
10. J. Mietz, S. Schneider, and F. Oeters, "Emulsification and mass transfer in ladle metallurgy," *Steel Research*, vol. 62, no. 1, pp. 10–15, 1991.
11. T. Wei and F. Oeters, "A model test for emulsion in gas-stirred ladles," *Steel Research*, vol. 63, no. 2, pp. 60–68, 1992.
12. S. L. Feldbauer, *Slag Entrainment in the Mold of a Continuous Caster*. PhD thesis, Carnegie Mellon University, 1995.
13. J. M. Harman and A. W. Cramb, "A study of the effect of fluid physical properties upon droplet emulsification," in *79th Steelmaking Conference Proceedings*, pp. 773–784, The Iron and Steel Society, 1996.
14. P. R. Scheller and R. Hagemann, "Model investigations on slag entrainment in continuous casting," *Archives of Metallurgy and Materials*, vol. 57, no. 1, pp. 283–289, 2012.
15. R. Hagemann, R. Schwarze, H. P. Heller, and P. R. Scheller, "Model investigations on the stability of the steel-slag interface in continuous-casting process," *Metallurgical and Materials Transactions B*, vol. 44, no. 1, pp. 80–90, 2013.
16. J. Savolainen, T. Fabritius, and O. Mattila, "Effect of fluid physical properties on the emulsification," *ISIJ International*, vol. 49, no. 1, pp. 29–36, 2009.
17. M. Iguchi, Y. Sumida, R. Okada, and Z.-I. Morita, "Evaluation of critical gas flow rate for the entrapment of slag using a water model," *ISIJ International*, vol. 34, no. 2, pp. 164–170, 1994.
18. K. Krishnapisharody, *Model Studies on Fluid Mechanic Interactions between Steel and Slag in Gas-Stirred Ladles*. PhD thesis, McMaster University, 2007.
19. K. Krishnapisharody and G. A. Irons, "Model studies on slag droplet generation in gas-stirred ladles," in *EPD Congress 2008, in Proceedings of The Minerals, Metals, and Materials Society 138th Annual Meeting*, pp. 293–302, The Minerals, Metals, and Materials Society, 2008.
20. K. Krishnapisharody and G. A. Irons, "Modeling and analysis of slag droplet formation in ladle metallurgy practice," in *Proceedings of AISTech 2008*, vol. 2, pp. 1243–1252, The Association for Iron and Steel Technology, 2008.
21. Z. Xiao, Y. Peng, and C. Liu, "Modelling study of the entrapment phenomena at the slag-metal interface in the gas-stirred ladle," *Chinese Journal of Metal Science and Technology*, vol. 3, no. 4, pp. 187–193, 1987.
22. M. Iguchi, J. Yoshida, T. Shimizu, and Y. Mizuno, "Model study on the entrapment of mold powder into molten steel," *ISIJ International*, vol. 40, no. 7, pp. 685–691, 2000.
23. P. Sulasalmi, A. Kärnä, T. Fabritius, and J. Savolainen, "CFD model for emulsification of slag into the steel," *ISIJ International*, vol. 49, no. 11, pp. 1661–1667, 2009.
24. A. Senguttuvan and G. A. Irons, "Model studies on slag metal entrainment in gas-stirred ladles," in *Proceedings of AISTech 2013*, pp. 1231–1241, The Association for Iron and Steel Technology, 2013.
25. L. Jonsson and P. Jönsson, "Modeling of fluid flow conditions around the slag/metal interface in a gas-stirred ladle," *ISIJ International*, vol. 36, no. 9, pp. 1127–1134, 1996.
26. K. Krishnapisharody and G. A. Irons, "Numerical simulation of droplet generation of the buoyant phase in two-phase liquid baths," in *EPD Congress 2008, in Proceedings of The Minerals, Metals, and Materials Society 138th Annual Meeting*, pp. 311–322, The Minerals, Metals, and Materials Society, 2008.
27. ANSYS Inc., Canonsburg, PA, *ANSYS FLUENT 14 Theory Guide*, 2011.
28. J. A. Dantzig and C. L. Tucker, *Modeling in Materials Processing*. Cambridge University Press, 2001.
29. F. R. Menter, "Two-equation eddy-viscosity turbulence models for engineering applications," *AIAA Journal*, vol. 32, no. 8, pp. 1598–1605, 1994.
30. C. W. Hirt and B. D. Nichols, "Volume of fluid (VOF) method for the dynamics of free boundaries," *Journal of Computational Physics*, vol. 39, no. 1, pp. 201–225, 1981.
31. J. U. Brackbill, D. B. Kothe, and C. Zemach, "A continuum method for modeling surface tension," *Journal of Computational Physics*, vol. 100, no. 2, pp. 335–354, 1992.
32. D. L. Youngs, "Time-dependent multi-material flow with large fluid distortion," in *Numerical Methods for Fluid Dynamics* (K. W. Morton and M. J. Baines, eds.), no. 24, pp. 273–285, New York: Academic Press, 1982.
33. R. I. Issa, "Solution of the implicitly discretised fluid flow equations by operator-splitting," *Journal of Computational Physics*, vol. 62, no. 1, pp. 40–65, 1986.